

Enhanced stability of 2D organic-inorganic halide perovskites by doping and heterostructure engineering

Rahul Singh,¹ Prashant Singh² and Ganesh Balasubramanian³

¹Department of Mechanical Engineering, Iowa State University, Ames, IA 50011

²Division of Materials Science & Engineering, Ames Laboratory, Ames, Iowa 50011,
USA

³Department of Mechanical Engineering & Mechanics, Lehigh University, Bethlehem,
PA 18015

Abstract

Organic-inorganic halide perovskite solar cells have recently attracted much attention due to their low-cost fabrication, flexibility, and high-power conversion efficiency. The reduction from three- to two-dimension (2D) promises an exciting opportunity to tune the electronic properties of organic-inorganic halide perovskites. Here, we propose first-principles density-functional theory based route to study the effect of reduced dimensionality, impurity doping, and heterostructure engineering on energy stability, band-gap and transport properties of 2D hybrid organic-inorganic halide perovskites. We show that the energetic stability of two-dimensional organic-inorganic halide perovskites can be significantly enhanced by chemically depositing MoS₂ monolayer as a precursor in the system by heterostructure engineering. While on one hand, the structures have similar and excellent transport properties as their bulk counterparts, on the other, they possess the advantage of a broad range of tunable band gaps. Our predictions will expedite future efforts (both theoretical and experimental) in the synthesis, measurements and applications of high performance perovskites.

Over the last decade, perovskites have been one of the most intensively examined classes of materials because of their outstanding optoelectronic properties.¹⁻⁶ The versatility of these materials encompasses a series of optoelectronic devices such as light-emitting diodes,^{1,2} transistors,³ lasing applications⁴, as well as other intriguing electronic properties.⁵⁻¹¹ In particular, organic-inorganic halide perovskites (OIHP), archetypically $\text{CH}_3\text{NH}_3\text{PbX}_3$ ($\text{X} = \text{Cl}, \text{Br}$ or I), have attracted significant attention because of their remarkable photovoltaic properties,¹²⁻¹⁴ achieving power conversion efficiency as high as 22.1%.⁴ Thin OIHP films that are typically synthesized and examined for the electronic transport, suffer from stability issues. A potential solution is to employ planar heterostructures in lieu of the 3-dimensional (3D i.e., bulk) films.^{13,15-23} Quantum confinement effects in 2D chemistries increase the band gap due to a blue shift that decreases with increasing number of layers in a heterostructured material.²⁴⁻²⁷ While increasing the number of inorganic layers decreases the bandgap, simultaneously it is detrimental to the stability.

Renewed interest in thermoelectrics is motivated by the realization that complexity at multiple length scales can lead to new mechanisms for high *performance perovskite* materials. Theoretical predictions suggested that the thermoelectric efficiency could be greatly enhanced by quantum confinement²⁸ by ionic doping or heterostructure engineering.²⁹⁻³⁰ The heterovalent or isovalent metal ions such as (Sn^{2+} , Cd^{2+} , Zn^{2+} , Mn^{2+})^{31,32-34} have been introduced as dopants with the possibility of imparting paramagnetism to increase stability. The heterostructure engineering by chemical layer deposition has also been tried to enhance the photoluminescence,³⁵ charge-transfer mechanism,³⁵ and surface dopant.³⁶ Both doping and chemical layer deposition can lead to quantum confinement (QC) of charges. The QC helps narrowing down electron energy bands with the decreasing dimensionality, which produces high effective masses and Seebeck coefficients. Moreover, similar sized heterostructures decouple the Seebeck coefficient and electrical conductivity by electron filtering³⁷ that could result in improved performance. Despite all the progress, our theoretical understanding of doping and

heterostructure engineering effect on underlying electronic and transport properties of perovskites is sparse and limited.

We employ first-principles density functional theory (DFT) to examine the stability, electronic-structure and transport properties of [001] terminated 2D OIHPs.³⁸ To test our hypothesis that ionic doping and inclusion of a MoS₂ML precursor can improve stability of OIHPs, we stack 2D assemblies of MAPbI₃ on top of MoS₂ML by constraining them within the interaction distances. Our results reveal that a single sheet of MoS₂ML considerably improves the power factor (*PF*) of OIHPs. The enhanced stability of the hybrid OIHPs is explained via the structural and electronic properties. In addition, we investigate the effect of magnetic impurity (Mn²⁺) doping on thermoelectric (TE) properties of 2D MAPbI₃ heterostructures, as a potential route to modulate the optical properties of halide perovskites.

We examine bulk and 2D variants of MA(Pb/Sn)I₃ OIHPs using first-principles density functional theory (DFT)^{39,40} based Vienna ab initio simulation package (VASP).^{41–43} We construct [001] terminated 2D OIHPs from 3D MA(Pb/Sn)I₃. For geometry optimization and electronic structure calculations, we use the projected augmented-wave (PAW) basis⁴⁴ and the Perdew–Burke–Ernzerhof (PBE)⁴¹ exchange-correlation functional. The charge and forces are converged to 10⁻⁵ eV and 0.01eV/Å, respectively, using energy cut-off of 800 eV. The Monkhorst-Pack⁴⁴ k-mesh grid of 7×7×3, and 3×3×5 is used for (2D MAPbI₃, 2D MASnI₃, Mn-doped-MAPbI₃) and MAPbI₃ML/MoS₂ML, respectively. The tetrahedron method with Blöchl corrections is used to calculate the density of states (DOS).⁴¹ The thermoelectric properties are calculated using the BoltzTrap⁴⁵ code interfaced with VASP.

Structural analysis of bulk and 2D variants of MAXI₃ (X=Pb, Sn): Hybrid organic-inorganic perovskites have an ABX₃ architecture, where A is a monovalent organic cation, CH₃NH₃⁺ (i.e., MA⁺), while B is a metal cation (i.e., Pb²⁺, Sn²⁺), and X is a halide anion (i.e., Cl, Br, I or their mixtures). In typical perovskite crystals, B occupies the center of an octahedral [BX₆]⁴⁶ cluster, while A is 12-fold cuboctahedrally coordinated with X anions.^{15,47} Similar to previous studies, we consider the high temperature pseudo-cubic phase of MAPbI₃.^{48,49} The calculated (experimental)^{50,51} lattice constants of bulk MAPbI₃

are $a = 6.432$ (6.361) Å, $b = 6.516$ (6.361) Å, $c = 6.446$ (6.361) Å, and $\alpha \approx \beta \approx \gamma \approx 90^\circ$. The predictions indicate a 3.41% increase in the simulated equilibrium cell volume relative to that in the experiments,^{50,51} with 1.27% increase in average bond length of Pb-I atoms. For 2D MAPbI₃, the calculated (experimental) lattice parameters of the PbI₂ surface are: $a = 6.437$ (6.361) Å and $b = 6.449$ (6.361) Å, respectively. We find a 1.38% increase in lattice constant in [110] plane of the simulated materials, although the thickness of the slab shrinks by 2.5%. The reduced thickness (Fig. 1 (c)) of the slab shrinks the overall slab volume by 1.33% with respect to experimental bulk MAPbI₃.

In case of Mn-doped 2D MAPbI₃, the calculated (experimental^{48,49}) lattice parameters are: $a = 6.361$ (6.361) Å and $b = 6.445$ (6.361) Å, respectively. The doped structure shows 25% distortion in Mn-I polyhedra, while only 9% distortion in Pb-I polyhedra. The average Mn-I bond-length increases by 4% relative to Pb-I. However, for MoS₂ML/MAPbI₃ML, $a = 6.362$ (6.361^{48,49}) Å and $b = 6.428$ (6.361^{48,49}) Å, respectively, similar to that of bulk MAPbI₃. The average Pb-I bond length is 3.201 Å similar to the value obtained in the bulk MAPbI₃. Also, MoS₂ML/MAPbI₃ML surface has negligible PbI₂ polyhedral distortion, which suggests of the structural stability of MAPbI₃ML “on surface disposition”. The structural differences caused by MoS₂ML enhances the stability of the system as noted from the relative energies of the six structures shown in Fig. 2.

Electronic properties of bulk and 2D variants of MAXI₃ (X=Pb, Sn): Experimentally, the bandgap of cubic MAPbI₃ is ~ 1.5 -1.62 eV.⁷ Our standard PBE calculations predict that bulk MAPbI₃ is a semiconductor with a direct bandgap of 1.726 eV, which agrees reasonably with the experiments. Using PBE electronic structure predictions as a reference, we perform additional band structure calculation of 2D MAPbI₃. The results indicate that both surfaces have a direct bandgap with the conduction band minimum (CBM) and valence band maximum (VBM) located at the M point of the Brillouin zone, as illustrated in Fig. 3. The energy states ranging from -3 to 3 eV are mostly contributed by Pb and I atoms, signifying their influence in the physical and chemical properties of these perovskites. Specifically, the states near the top of the valence band are predominated by I-5*p* and Pb-6*s* states, while the conduction bands are constituted by Pb-6*p* states with hybridization of I-5*p* states. As shown earlier in Fig.1, the surface terminated by PbI₂

contains more Pb atoms, which leads to a broader conduction band and thus a narrower bandgap of the 2D MAPbI₃ terminated by PbI₂.

The spin-polarized band structure for 10% Mn-doped 2D MAPbI₃ are presented in Fig. 4 (a). The bandgap of the Mn-doped OIHP at Pb-site is 1.2 eV, while Mn at Sn site reduces the bandgap to ~ 1 eV (below, we discuss only Mn-doping at Pb-site). Both the top of the valence band and the bottom of the conduction band are located at the M [$\frac{1}{2}$ $\frac{1}{2}$ 0] point. The doping results in a more stable structure by distorting the neighboring environment, see charge density plot in Fig. 4 (b) (top), compared to pure 2D structures (Fig. 2). However, the bandgap of Mn-doped OIHP decreases due to large structural distortion. The Mn spin-up channel is completely filled, and down-spin channel is completely empty leading to strong magnetic behavior (Mn-moment $\sim 5 \mu_B$) as shown by magnetization density plot in Fig. 4 (b) (bottom). The top flat band just below the Fermi level, corresponds to the Mn impurity band, which is attributed to the Mn-3*d* state. The Mn-doping changes the electronic structure near the Fermi level affecting stability as well as the transport properties. While there is no notable improvement in transport properties, the stability of the structure is enhanced by Mn-doping.

Next, we investigate the effect of charge-transfer interactions in MoS₂ML/MAPbI₃ML. The adsorption of organic molecules is expected to modify the electronic properties of MoS₂ML. The MoS₂ML isolated layer has a predicted direct bandgap of 1.73 eV, closer to the experimentally observed observation band-gap of 1.70 eV.^{52,53} The VBM of MoS₂ML is contributed by Mo-4*d* and S-3*p* states, while the CBM is mainly contributed by Mo-4*d* states and feebly by S-3*p* states.

To obtain a deeper insight into the electronic properties of the now functionalized MoS₂ML, we compute the density of states (DOS) and full charge densities (projected and full, which includes VBM and CBM) for MoS₂ML/MAPbI₃ML, illustrated in Figure 5. The adsorption of MAPbI₃ML introduces new flat energy levels in the bandgap region of MoS₂ML resulting in a bandgap of ~ 1.27 eV. As the interactions between MAPbI₃ML and MoS₂ML are weak, the band structure of functionalized MoS₂ML is effectively a combination of those of MoS₂ML and the adsorbed MAPbI₃ML. Hence, the bandgap

reduction is attributed to the recombination of the energy levels. Nevertheless, for MAPbI₃ML functionalized MoS₂ML, the new energy levels appear in the region of the conduction band, indicating that MoS₂ML can be tuned into a p-type semiconductor by doping with MAPbI₃ML. As shown in Fig. 5 (right-panel), for MoS₂ML/MAPbI₃ML both CBM and VBM are solely contributed by MAPbI₃ML. In the band-structure plot, MoS₂ predominantly lies below -0.2 eV with respect to the Fermi level, E_F. The conduction bands with an energy range from ~1 - 3 eV are derived largely from the Pb-*s/p* and I-*s* states. The valence bands with a range from -3 eV – 0 eV exert strong hybridization between the Pb-*p*, I-*p*, Mo-*d* and S-*p* states. The localized distribution of electron density on MAPbI₃ML and MoS₂ML indicates negligible effect of the interlayer interactions but is responsible for higher stability of MoS₂ML/MAPbI₃ML as compared to the bulk structure. The weaker interaction, in Fig. 5 (c), is shown by small band-distortion at the interface of MoS₂ML and MAPbI₃ML, where bond-angle between Pb-I-Pb changes from 180° to ~179°. We also note from this structural analysis that band-distortions are reduced to ~5% in MoS₂ML/MAPbI₃ML compared to ~10-20% in MAPbI₃ML or Mn-doped MAPbI₃ML.

Thermoelectric properties of bulk and 2D variants of MAXI₃ (X=Pb, Sn): A band-structure possessing a large-effective mass in CBM, with a minimum of about $5k_B T$ above the VBM, can potentially achieve nonmonotonic Seebeck coefficient, and hence a large PF .⁵⁴ Deposition of MAPbI₃ML on MoS₂ML introduces resonant states that can achieve a tailored band structure. We determine the band effective mass, m^* from second order derivative of the band energy with respect to the wave vectors:

$$\left(\frac{1}{m^*}\right) = \frac{1}{\hbar^2} \frac{\partial^2 E_n}{\partial k_x \partial k_y}$$

where, x and y are the directions in reciprocal space, n is the band index, E_n is the band energy, and \hbar is the modified Planck's constant. The derivatives have been evaluated at CBM for electrons (m^e) and at VBM for holes (m^h). The reduction in dimensions from bulk to 2D creates opportunities to optimize the highly anisotropic structures due to the smaller directional effective mass (electrical conductivity, $\sigma \propto \frac{1}{m^*}$).⁵⁵

The calculated effective hole/electron mass for bulk MAPbI₃ is $(0.17; 0.19; 0.28)m_h^*$ and $(0.27; 1.51; 0.12)m_e^*$, respectively. The three values in the parentheses represent the three perpendicular directions (x, y, z), while for 2D structures we consider the two planar directions (x, y). For 2D MAPbI₃, the corresponding values are $(0.17; 0.33)m_h^*$ and $(1.53; 0.85)m_e^*$, respectively. The calculated effective mass for 2D MAPbI₃ indicates an obvious in-plane anisotropy in effective mass due to [100] stacking. The strong directional effective mass is larger along [100] stacking, and the direction orthogonal to the stacking [010] predicts smaller values. Thus, we deduce that the carrier mobility is high (small effective mass) along [010], with heavy mass states present in the transverse direction, i.e., [100]. Similarly, the Mn-doped 2D MAPbI₃ shows large anisotropy in effective mass along [100] stacking at Pb-site $[(0.12; 5.42)m_h^*, (2.50; 1.15)m_e^*]$. In contrast to the Mn-doped 2D MAPbI₃, the energy minima/maxima shift to the X $[\frac{1}{2} 0 0]$ point from the M point in MoS₂ML/MAPbI₃ML. The calculated hole- and electron-effective masses at M-point are $m_h^* = (0.76; 1.13)$ and $m_e^* = (3.40; 1.51)$, respectively. The large anisotropy in the effective mass along the [100] direction facilitates hole transport holes along [100] compared to the electrons. However, along the [010] direction, both electrons and holes experience equal effective mass resulting in similar transport properties.

In TE materials, a high Seebeck coefficient (S) at a given carrier concentration results from a high overall DOS effective mass (m_d^*). However, σ decreases with increasing m_d^* , and also depends on the inertial effective mass, m^* . Ioffe showed empirically that for doped semiconductors to be good TEs, the sweet-spot for carrier concentration, $n \sim 10^{18} - 10^{20}$ per cm³, corresponding to degenerate semiconductors or semimetals.⁵⁶ Here, we predict a similar range for n_{hole} and n_{electron} . As the doping concentration increases, σ increases and S decreases. Figs. 6 (a) and (b) present S predictions for 2D MAPbI₃ (left-panel) and MoS₂ML/MAPbI₃ML (right-panel). In comparison with bulk MAPbI₃,⁵⁷ we find that S of 2D MAPbI₃ is $\sim 20\%$ lower.⁵⁷ The large S in bulk MAPbI₃ arises from the DOS and band mobility. As shown earlier in Fig. 3, the DOS above and below the Fermi level have a significant contrast in the bulk structures⁵³ compared to the 2D counterparts, and the smaller m^* in 3D materials leads to an increased band mobility⁵⁷ that is important to enhance the electronic transport. In Fig. 6, we show that bulk MAPbI₃ has slightly better

TE properties than 2D MAPbI₃ and MoS₂ML/MAPbI₃ML, however, 2D counterparts have better energetic stability (see Fig. 2). For all practical purposes, the latter is more important, as stability of materials signifies that 2D MAPbI₃/MoS₂ML/MAPbI₃ML can be formed in a laboratory environment and will not degrade as quickly as bulk MAPbI₃.⁴⁷

$PF = S^2\sigma$ of a TE material quantifies their electrical power generation ability. The most efficient TE materials possess high σ and high S . Since σ and S have competing dependencies on n simultaneously obtaining high values for both properties is challenging. We compare the calculated PF per relaxation time as a function of temperature for MAPbI₃ML and that with MoS₂ML. Although both materials originate from the parent cubic crystal structure, differences are noted in their TE properties (Figs. 6(a)–(f)). The dissimilarities in σ of 2D MAPbI₃ and MoS₂ML/MAPbI₃ML originates from latter's intrinsic sp -type bonding. The 2D OIHP deposited on MoS₂ has slightly lower $PF \sim 29.3 \times 10^{10}$ W/m.K².s relative to 2D MAPbI₃ ($\sim 32.5 \times 10^{10}$ W/m.K².s) due to an enhanced thermal electronic conductivity.⁵⁷ Both 2D MAPbI₃ and MoS₂ML/MAPbI₃ML show strong temperature dependence in S , but σ essentially remains temperature invariant. Thus, the PF predictions for specific chemical potential value at 800 K, Fig. 6 (e) and (f), are $\sim 100\%$ and $\sim 200\%$ higher than at 500 and 300 K, respectively, for both materials. Note that PF of 2D MAPbI₃ is $\sim 10\%$ higher than MoS₂ML/MAPbI₃ML, but an enhanced energetic stability of the latter contributes to its selection for potential TE applications. On one hand, OIHPs possess the advantage of hybridization, while on the other hand, they demonstrate the ability to tune TE properties through nanostructuring. In addition, the PF can be further tuned by controlling the ionic doping concentrations.

In this paper, we propose approaches to manipulate the electronic and thermoelectric properties of 2D OIHPs. From first-principles calculations, we show that energetic stability of 2D OIHPs and its variants can be tuned by impurity doping and by monolayer deposition. Our findings show that the chemically deposited monolayer of 2D MAPbI₃ on MoS₂ provides optimal bandgap required for photovoltaic applications. The enhanced bandgap, compared to 2D MAPbI₃, arises from the weak interactions between MoS₂ and MAPbI₃ monolayers. Moreover, the weak interlayer interactions energetically stabilize MoS₂ML/MAPbI₃ML. The MoS₂ML/MAPbI₃ML also possesses the excellent

thermoelectric properties as noted in bulk MAPbI₃. We believe our predictions provide a useful guideline for future experiments examining the stability of OIHP based solar materials and suggest a practicable approach to enhance the light-harvesting capability of MoS₂ML/MAPbI₃ML.

Acknowledgment

The research was supported, in part, by the National Science Foundation (NSF) grant no. CMMI-1404938. The work at Ames Laboratory was supported by the U.S. Department of Energy (DOE), Office of Science, Basic Energy Sciences, Materials Science & Engineering Division, which is operated by Iowa State University for the U.S. DOE under contract DE-AC02-07CH11358.

References

- (1) Jaramillo-Quintero, O. A.; Sanchez, R. S.; Rincon, M.; Mora-Sero, I. Bright Visible-Infrared Light Emitting Diodes Based on Hybrid Halide Perovskite with Spiro-OMeTAD as a Hole-Injecting Layer. *J. Phys. Chem. Lett.* **2015**, *6* (10), 1883–1890.
- (2) Tan, Z.-K.; Moghaddam, R. S.; Lai, M. L.; Docampo, P.; Higler, R.; Deschler, F.; Price, M.; Sadhanala, A.; Pazos, L. M.; Credgington, D.; et al. Bright Light-Emitting Diodes Based on Organometal Halide Perovskite. *Nat. Nanotechnol.* **2014**, *9* (9), 687–692.
- (3) Chin, X. Y.; Cortecchia, D.; Yin, J.; Bruno, A.; Soci, C. Lead Iodide Perovskite Light-Emitting Field-Effect Transistor. *Nat. Commun.* **2015**, *6* (1).
- (4) Xing, G.; Mathews, N.; Sun, S.; Lim, S. S.; Lam, Y. M.; Gratzel, M.; Mhaisalkar, S.; Sum, T. C. Long-Range Balanced Electron- and Hole-Transport Lengths in Organic-Inorganic CH₃NH₃PbI₃. *Science* **2013**, *342* (6156), 344–347.
- (5) Jung, H. S.; Park, N.-G. Perovskite Solar Cells: From Materials to Devices. *Small* **2015**, *11* (1), 10–25.
- (6) Kojima, A.; Teshima, K.; Shirai, Y.; Miyasaka, T. Organometal Halide Perovskites as Visible-Light Sensitizers for Photovoltaic Cells. *J. Am. Chem. Soc.* **2009**, *131* (17), 6050–6051.
- (7) Ogomi, Y.; Morita, A.; Tsukamoto, S.; Saitho, T.; Fujikawa, N.; Shen, Q.; Toyoda, T.; Yoshino, K.; Pandey, S. S.; Ma, T.; et al. CH₃NH₃Sn_xPb_(1-x)I₃ Perovskite Solar Cells Covering up to 1060 Nm. *J. Phys. Chem. Lett.* **2014**, *5* (6), 1004–1011.
- (8) Snaith, H. J. Perovskites: The Emergence of a New Era for Low-Cost, High-Efficiency Solar Cells. *J. Phys. Chem. Lett.* **2013**, *4* (21), 3623–3630.
- (9) Song, T.-B.; Chen, Q.; Zhou, H.; Jiang, C.; Wang, H.-H.; (Michael) Yang, Y.; Liu, Y.; You, J.; Yang, Y. Perovskite Solar Cells: Film Formation and Properties. *J. Mater. Chem. A* **2015**, *3* (17), 9032–9050.
- (10) Sum, T. C.; Mathews, N. Advancements in Perovskite Solar Cells: Photophysics behind the Photovoltaics. *Energy Env. Sci* **2014**, *7* (8), 2518–2534.
- (11) Weber, D. CH₃NH₃PbX₃, ein Pb(II)-System mit kubischer Perowskitstruktur / CH₃NH₃PbX₃, a Pb(II)-System with Cubic Perovskite Structure. *Z. Für Naturforschung B* **1978**, *33* (12).

- (12) Sessolo, M.; Bolink, H. J. Perovskite Solar Cells Join the Major League. *Science* **2015**, *350* (6263), 917–917.
- (13) Stranks, S. D.; Snaith, H. J. Metal-Halide Perovskites for Photovoltaic and Light-Emitting Devices. *Nat. Nanotechnol.* **2015**, *10* (5), 391–402.
- (14) Yang, W. S.; Park, B.-W.; Jung, E. H.; Jeon, N. J.; Kim, Y. C.; Lee, D. U.; Shin, S. S.; Seo, J.; Kim, E. K.; Noh, J. H.; et al. Iodide Management in Formamidinium-Lead-Halide-Based Perovskite Layers for Efficient Solar Cells. *Science* **2017**, *356* (6345), 1376–1379.
- (15) Berry, J.; Buonassisi, T.; Egger, D. A.; Hodes, G.; Kronik, L.; Loo, Y.-L.; Lubomirsky, I.; Marder, S. R.; Mastai, Y.; Miller, J. S.; et al. Hybrid Organic-Inorganic Perovskites (HOIPs): Opportunities and Challenges. *Adv. Mater.* **2015**, *27* (35), 5102–5112.
- (16) Burschka, J.; Pellet, N.; Moon, S.-J.; Humphry-Baker, R.; Gao, P.; Nazeeruddin, M. K.; Grätzel, M. Sequential Deposition as a Route to High-Performance Perovskite-Sensitized Solar Cells. *Nature* **2013**, *499* (7458), 316–319.
- (17) Green, M. A.; Ho-Baillie, A.; Snaith, H. J. The Emergence of Perovskite Solar Cells. *Nat. Photonics* **2014**, *8* (7), 506–514.
- (18) Heo, J. H.; Im, S. H.; Noh, J. H.; Mandal, T. N.; Lim, C.-S.; Chang, J. A.; Lee, Y. H.; Kim, H.; Sarkar, A.; Nazeeruddin, M. K.; et al. Efficient Inorganic–Organic Hybrid Heterojunction Solar Cells Containing Perovskite Compound and Polymeric Hole Conductors. *Nat. Photonics* **2013**, *7* (6), 486–491.
- (19) Huang, X.; Zhao, Z.; Cao, L.; Chen, Y.; Zhu, E.; Lin, Z.; Li, M.; Yan, A.; Zettl, A.; Wang, Y. M.; et al. High-Performance Transition Metal-Doped Pt₃Ni Octahedra for Oxygen Reduction Reaction. *Science* **2015**, *348* (6240), 1230–1234.
- (20) Im, J.-H.; Jang, I.-H.; Pellet, N.; Grätzel, M.; Park, N.-G. Growth of CH₃NH₃PbI₃ Cuboids with Controlled Size for High-Efficiency Perovskite Solar Cells. *Nat. Nanotechnol.* **2014**, *9* (11), 927–932.
- (21) Liu, D.; Kelly, T. L. Perovskite Solar Cells with a Planar Heterojunction Structure Prepared Using Room-Temperature Solution Processing Techniques. *Nat. Photonics* **2014**, *8* (2), 133–138.

- (22) Mei, A.; Li, X.; Liu, L.; Ku, Z.; Liu, T.; Rong, Y.; Xu, M.; Hu, M.; Chen, J.; Yang, Y.; et al. A Hole-Conductor-Free, Fully Printable Mesoscopic Perovskite Solar Cell with High Stability. *Science* **2014**, *345* (6194), 295–298.
- (23) Wehrenfennig, C.; Eperon, G. E.; Johnston, M. B.; Snaith, H. J.; Herz, L. M. High Charge Carrier Mobilities and Lifetimes in Organolead Trihalide Perovskites. *Adv. Mater.* **2014**, *26* (10), 1584–1589.
- (24) Dou, L.; Wong, A. B.; Yu, Y.; Lai, M.; Kornienko, N.; Eaton, S. W.; Fu, A.; Bischak, C. G.; Ma, J.; Ding, T.; et al. Atomically Thin Two-Dimensional Organic-Inorganic Hybrid Perovskites. *Science* **2015**, *349* (6255), 1518–1521.
- (25) Goldschmidt, V. M. Die Gesetze der Krystallochemie. *Naturwissenschaften* **1926**, *14* (21), 477–485.
- (26) Ma, L.; Dai, J.; Zeng, X. C. Two-Dimensional Single-Layer Organic-Inorganic Hybrid Perovskite Semiconductors. *Adv. Energy Mater.* **2017**, *7* (7), 1601731.
- (27) Pandey, M.; Jacobsen, K. W.; Thygesen, K. S. Band Gap Tuning and Defect Tolerance of Atomically Thin Two-Dimensional Organic-Inorganic Halide Perovskites. *J. Phys. Chem. Lett.* **2016**, *7* (21), 4346–4352.
- (28) Hicks, L. D.; Dresselhaus, M. S. Effect of Quantum-Well Structures on the Thermoelectric Figure of Merit. *Phys. Rev. B* **1993**, *47* (19), 12727–12731.
- (29) Chen, W.; Chen, S.; Qi, D. C.; Gao, X. Y.; Wee, A. T. S. Surface Transfer P-Type Doping of Epitaxial Graphene. *J. Am. Chem. Soc.* **2007**, *129* (34), 10418–10422.
- (30) Samuels, A. J.; Carey, J. D. Molecular Doping and Band-Gap Opening of Bilayer Graphene. *ACS Nano* **2013**, *7* (3), 2790–2799.
- (31) van der Stam, W.; Geuchies, J. J.; Altantzis, T.; van den Bos, K. H. W.; Meeldijk, J. D.; Van Aert, S.; Bals, S.; Vanmaekelbergh, D.; de Mello Donega, C. Highly Emissive Divalent-Ion-Doped Colloidal $\text{CsPb}_{1-x}\text{M}_x\text{Br}_3$ Perovskite Nanocrystals through Cation Exchange. *J. Am. Chem. Soc.* **2017**, *139* (11), 4087–4097.
- (32) Das Adhikari, S.; Dutta, S. K.; Dutta, A.; Guria, A. K.; Pradhan, N. Chemically Tailoring the Dopant Emission in Manganese-Doped CsPbCl_3 Perovskite Nanocrystals. *Angew. Chem. Int. Ed.* **2017**, *56* (30), 8746–8750.
- (33) Huang, G.; Wang, C.; Xu, S.; Zong, S.; Lu, J.; Wang, Z.; Lu, C.; Cui, Y. Postsynthetic Doping of MnCl_2 Molecules into Preformed CsPbBr_3 Perovskite

- Nanocrystals via a Halide Exchange-Driven Cation Exchange. *Adv. Mater.* **2017**, *29* (29), 1700095.
- (34) Parobek, D.; Roman, B. J.; Dong, Y.; Jin, H.; Lee, E.; Sheldon, M.; Son, D. H. Exciton-to-Dopant Energy Transfer in Mn-Doped Cesium Lead Halide Perovskite Nanocrystals. *Nano Lett.* **2016**, *16* (12), 7376–7380.
- (35) Mouri, S.; Miyauchi, Y.; Matsuda, K. Tunable Photoluminescence of Monolayer MoS₂ via Chemical Doping. *Nano Lett.* **2013**, *13* (12), 5944–5948.
- (36) Kiriya, D.; Tosun, M.; Zhao, P.; Kang, J. S.; Javey, A. Air-Stable Surface Charge Transfer Doping of MoS₂ by Benzyl Viologen. *J. Am. Chem. Soc.* **2014**, *136* (22), 7853–7856.
- (37) Zide, J. M. O.; Vashaee, D.; Bian, Z. X.; Zeng, G.; Bowers, J. E.; Shakouri, A.; Gossard, A. C. Demonstration of Electron Filtering to Increase the Seebeck Coefficient in In_{0.53}Ga_{0.47}As/In_{0.53}Ga_{0.28}Al_{0.19}As Superlattices. *Phys. Rev. B* **2006**, *74* (20).
- (38) Kohnehpoushi, S.; Nazari, P.; Nejand, B. A.; Eskandari, M. MoS₂ : A Two-Dimensional Hole-Transporting Material for High-Efficiency, Low-Cost Perovskite Solar Cells. *Nanotechnology* **2018**, *29*, 205201-.
- (39) Kresse, G.; Furthmüller, J. Efficiency of Ab-Initio Total Energy Calculations for Metals and Semiconductors Using a Plane-Wave Basis Set. *Comput. Mater. Sci.* **1996**, *6* (1), 15–50.
- (40) Kresse, G.; Furthmüller, J. Efficient Iterative Schemes for *Ab Initio* Total-Energy Calculations Using a Plane-Wave Basis Set. *Phys. Rev. B* **1996**, *54* (16), 11169–11186.
- (41) Blöchl, P. E. Projector Augmented-Wave Method. *Phys. Rev. B* **1994**, *50* (24), 17953–17979.
- (42) Kresse, G.; Hafner, J. Ab Initio Molecular Dynamics for Liquid Metals. *Phys. Rev. B* **1993** *47*, 558.
- (43) Perdew, J. P.; Burke, K.; Ernzerhof, M. Generalized Gradient Approximation Made Simple [Phys. Rev. Lett. *77*, 3865 (1996)]. *Phys. Rev. Lett.* **1997**, *78* (7), 1396–1396.
- (44) Monkhorst, H. J.; Pack, J. D. Special Points for Brillouin-Zone Integrations. *Phys. Rev. B*, **1976**, *13*, 5188--5192.

- (45) Madsen, G. K. H.; Singh, D. J. BoltzTraP. A Code for Calculating Band-Structure Dependent Quantities. *Comput. Phys. Commun.* **2006**, *175* (1), 67–71.
- (46) Stranks, S. D.; Eperon, G. E.; Grancini, G.; Menelaou, C.; Alcocer, M. J. P.; Leijtens, T.; Herz, L. M.; Petrozza, A.; Snaith, H. J. Electron-Hole Diffusion Lengths Exceeding 1 Micrometer in an Organometal Trihalide Perovskite Absorber. *Science* **2013**, *342* (6156), 341–344.
- (47) Leijtens, T.; Eperon, G. E.; Noel, N. K.; Habisreutinger, S. N.; Petrozza, A.; Snaith, H. J. Stability of Metal Halide Perovskite Solar Cells. *Adv. Energy Mater.* **2015**, *5* (20), 1500963.
- (48) Brivio, F.; Frost, J. M.; Skelton, J. M.; Jackson, A. J.; Weber, O. J.; Weller, M. T.; Goñi, A. R.; Leguy, A. M. A.; Barnes, P. R. F.; Walsh, A. Lattice Dynamics and Vibrational Spectra of the Orthorhombic, Tetragonal, and Cubic Phases of Methylammonium Lead Iodide. *Phys. Rev. B* **2015**, *92* (14).
- (49) Brivio, F.; Walker, A. B.; Walsh, A. Structural and Electronic Properties of Hybrid Perovskites for High-Efficiency Thin-Film Photovoltaics from First-Principles. *APL Mater.* **2013**, *1* (4), 042111.
- (50) Baikie, T.; Fang, Y.; Kadro, J. M.; Schreyer, M.; Wei, F.; Mhaisalkar, S. G.; Graetzel, M.; White, T. J. Synthesis and Crystal Chemistry of the Hybrid Perovskite (CH₃NH₃)PbI₃ for Solid-State Sensitised Solar Cell Applications. *J. Mater. Chem. A* **2013**, *1* (18), 5628.
- (51) Nandi, P.; Giri, C.; Joseph, B.; Rath, S.; Manju, U.; Topwal, D. CH₃NH₃PbI₃, A Potential Solar Cell Candidate: Structural and Spectroscopic Investigations. *J. Phys. Chem. A* **2016**, *120* (49), 9732–9739.
- (52) Splendiani, A.; Sun, L.; Zhang, Y.; Li, T.; Kim, J.; Chim, C.-Y.; Galli, G.; Wang, F. Emerging Photoluminescence in Monolayer MoS₂. *Nano Lett.* **2010**, *10* (4), 1271–1275.
- (53) Li, Y.; Li, Y.-L.; Araujo, C. M.; Luo, W.; Ahuja, R. Single-Layer MoS₂ as an Efficient Photocatalyst. *Catal. Sci. Technol.* **2013**, *3* (9), 2214.
- (54) Kim, R.; Lundstrom, M. S. Computational Study of the Seebeck Coefficient of One-Dimensional Composite Nano-Structures. *J. Appl. Phys.* **2011**, *110* (3), 034511.
- (55) Kittel, C. *Introduction to Solid State Physics*, 7th ed.; Wiley.

- (56) Ioffe, A. F.; Stil'bans, L. S.; Iordanishvili, E. K.; Stavitskaya, T. S.; Gelbtuch, A.; Vineyard, G. *Semiconductor Thermoelements and Thermoelectric Cooling. Phys. Today* **1959**, *12* (5), 42–42.
- (57) Singh, R.; Kottokaran, R.; Dalal, V. L.; Balasubramanian, G. Engineering Band Gap and Electronic Transport in Organic-Inorganic Halide Perovskites by Superlattices. *Nanoscale* **2017**, *9*, 8600-8607.

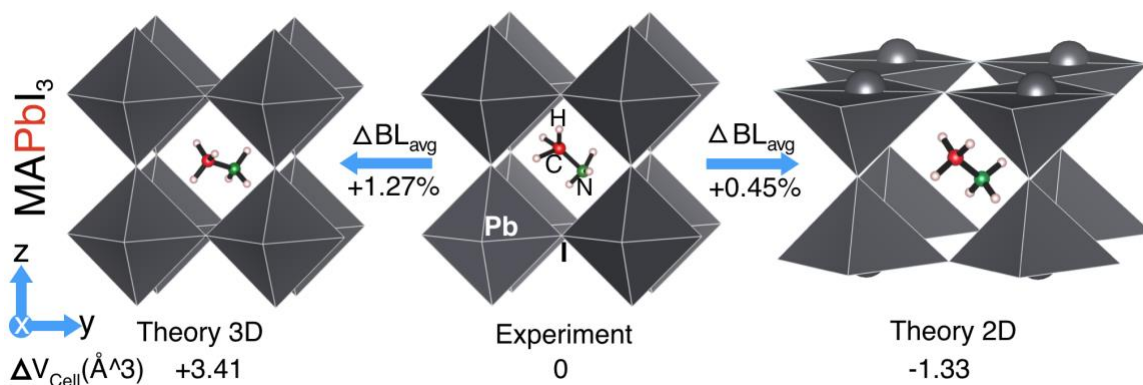


Figure 1: (Color online) The side view of bulk MAPbI_3 unit cell as obtained from (a) simulations and (b) experiments. The side view of (c) (001) terminated 2D MAPbI_3 unit cell. The unit cell volume of the bulk and energetically relaxed structure increases by 3.41% relative to the experimentally measured volume, while the 2D cell shrinks by 1.33%. In comparison to the experiments the average Pb-I bond-length of bulk and 2D MAPbI_3 increases by 1.27 and 0.45%, respectively. For the relaxed 2D MASnI_3 , the unit cell volume and average Sn-I bond length increases by 1.65 and 2.05%, respectively, compared to bulk (see supplement).

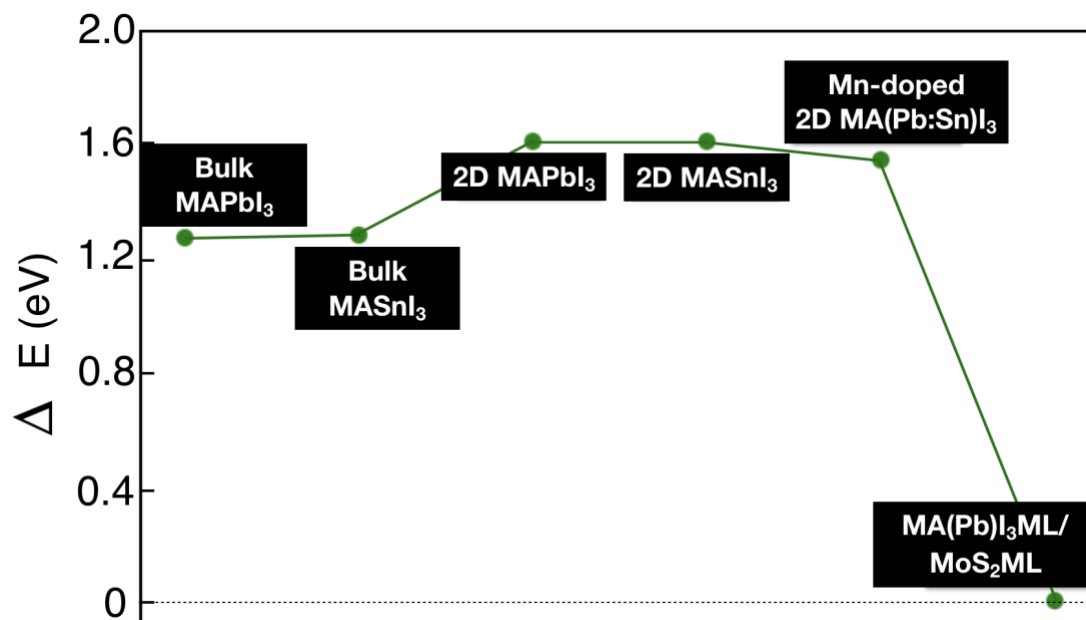


Figure 2: (Color online) Relative formation energies (eV) of bulk, 2D, Mn-doped and MAPbI₃ML/MoS₂ML MAPbI₃ suggest that the MAPbI₃ML/MoS₂ML offers the highest structural stability (lowest formation energy). ML stands for monolayer.

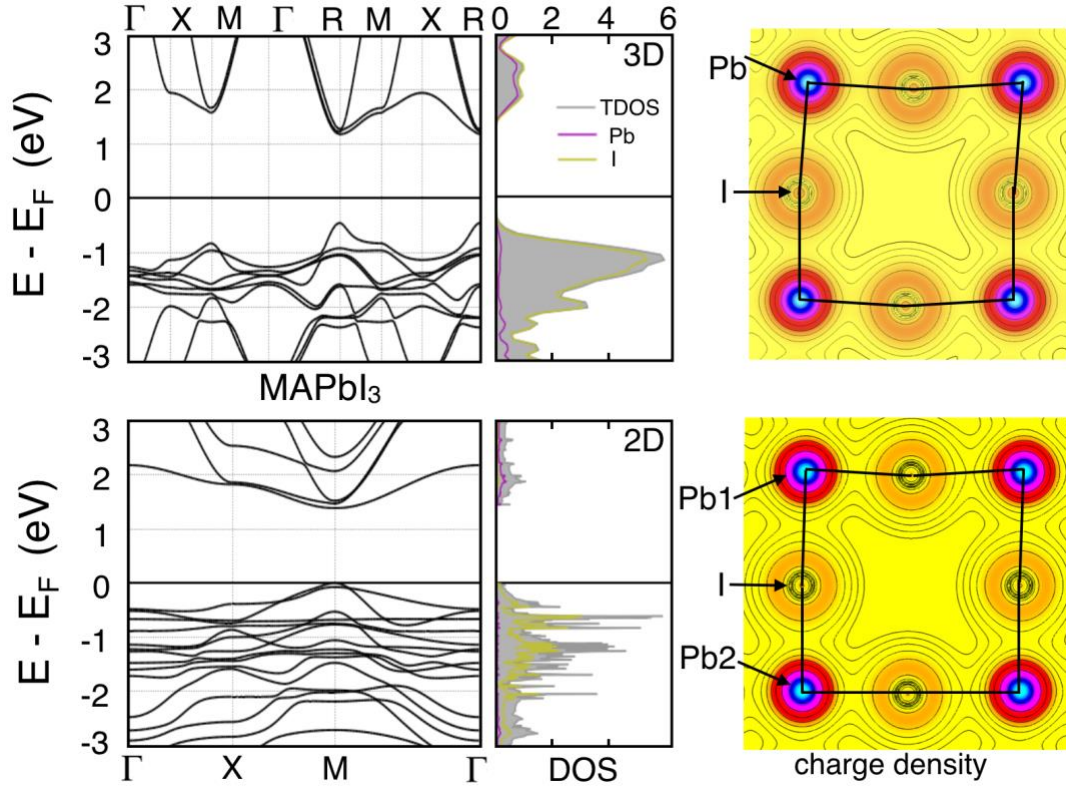


Figure 3: (Color online) Comparative band-structure, density of states (DOS) and (001) projected charge density of bulk and [001] terminated 2D MAPbI₃. We can see that going from bulk to 2D makes DOS more structured and bands flatter. Both bulk and 2D MAPbI₃ show calculated direct band-gap of 1.726 eV and 1.27 eV at R-point and M-point of Brillouin zone, respectively. The [001] projected charge density of 2D MAPbI₃ reveals enhanced bonding between Pb and I (as seen by non-circular lobes both at Pb and I-sites) compared to bulk. Identical isosurface values are employed for the charge density plots.

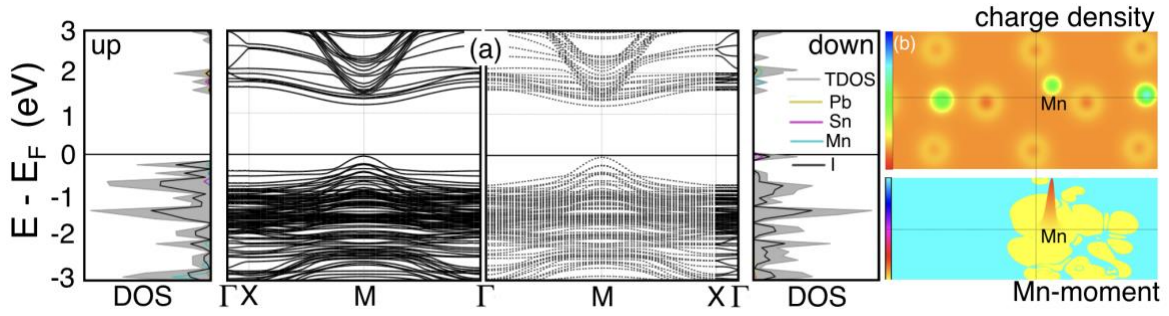


Figure 4: (Color online) (a) Spin-polarized band structure, (b) charge density (top) and magnetization density (bottom) of Mn-doped (at Pb-site) 2D MAPbI₃ monolayer stacked along [010] direction. In Mn-doped MA(Pb;Sn)I₃, the strong magnetic characteristic of Mn with high saturation magnetization of ~ 5 Bohr magneton (μ_B), leads to induced I moments on nearby sites by distortion of the MnI₂ polyhedra. Mn-doping stabilizes MAPbI₃ML almost by ~ 0.12 eV with respect to 2D MAPbI₃ and 2D MASnI₃ (see Fig. 2).

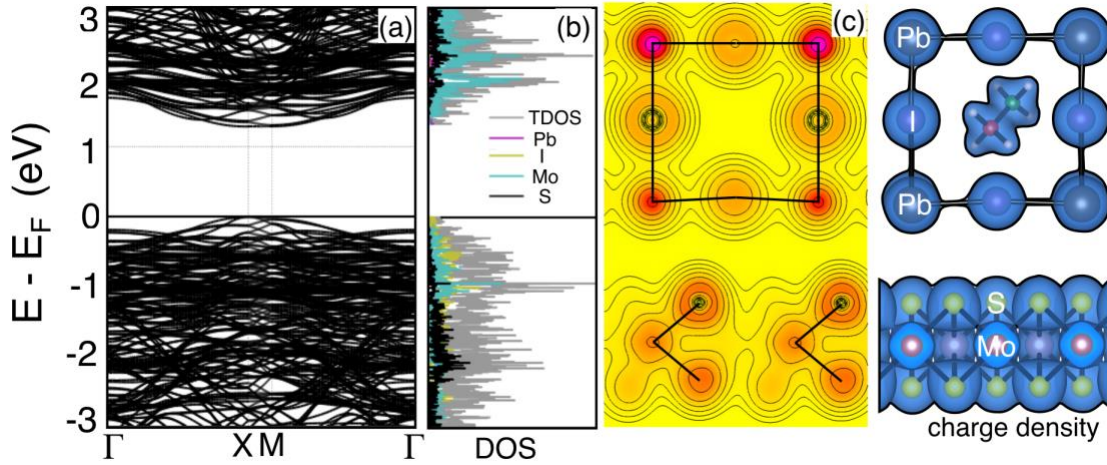


Figure 5: (Color online) (a) The electronic band-structure, (b) density of states (center), and (c) (110) projected and full charge density of chemically deposited MAPbI₃ monolayer (ML) on MoS₂ML. The MAPbI₃ML/MoS₂ML enhances the band gap to 1.27 eV with respect to Mn-doped MAPbI₃ML (see Figs. 4). Chemical layer deposition of MAPbI₃ML on MoS₂ML enhances energetic stability compared to bulk, 2D, and Mn-doped MA(Pb;Sn)I₃ML. We attribute increased stability to the weaker interlayer interaction originating from Pb-6*p* and S-3*p* states.

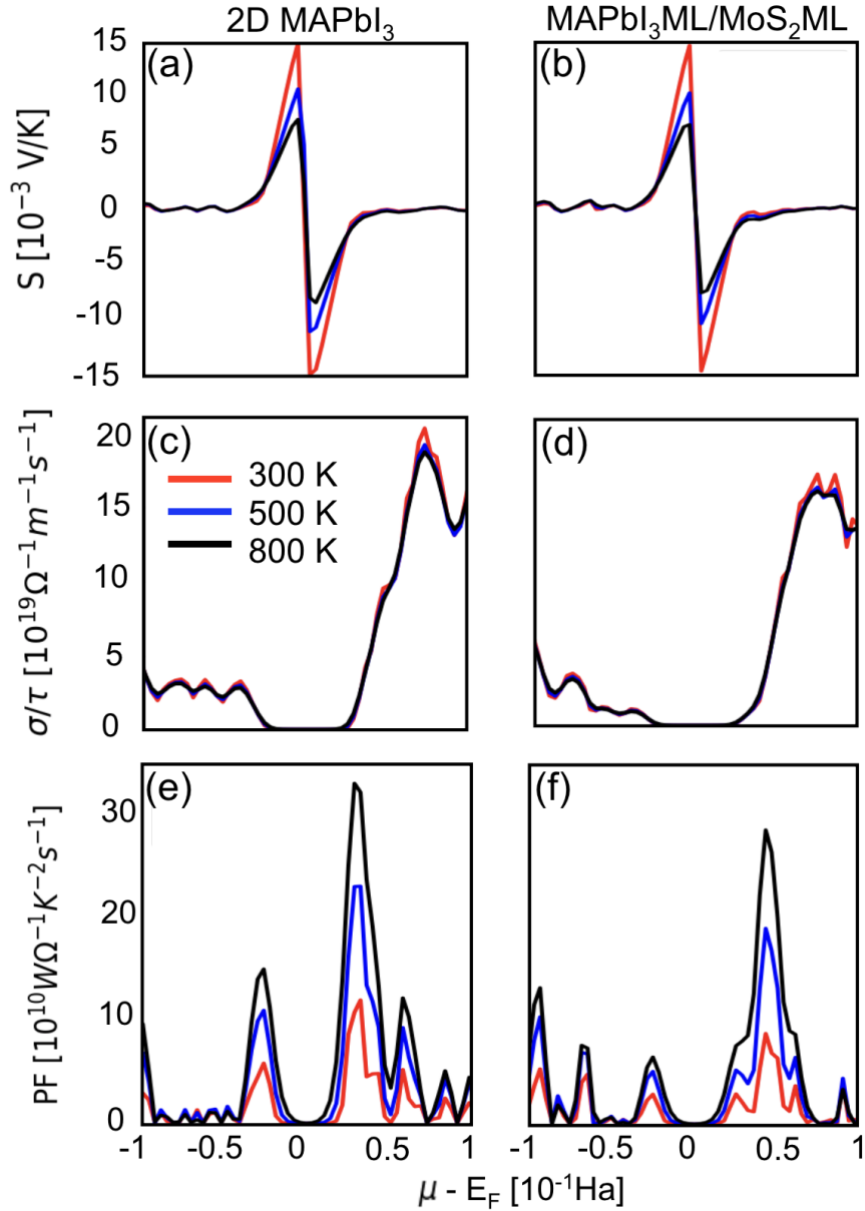


Figure 6: (Color online) The Seebeck coefficient (a, b), the electrical conductivity (c, d), and the power factor (e, f) of 2D MAPbI₃ (left-panel) and MAPbI₃ML/MoS₂ML (right panel) are presented at 300 K, 500 K and 800 K, respectively (ML = monolayer). The optimal value of power factor (e, f) for the two cases occur at a chemical potential of +0.025 and +0.04 Hartree, respectively. We show that MAPbI₃ML/MoS₂ML retain the thermoelectric properties of bulk with an order of magnitude increase in the energy stability (see Fig.2).⁵⁷